J. Fluid Mech. (1999), *vol.* 389, *pp.* 101–118. Printed in the United Kingdom

Oscillatory flow states in an enclosed cylinder with a rotating endwall

By J. L. STEVENS[1], J. M. LOPEZ[2] and B. J. CANTWELL[1]

[1] Department of Aeronautics and Astronautics, Stanford University, Stanford, CA 94305, USA

[2] Department of Mathematics, Arizona State University, Tempe, AZ 85287-1804, USA

(Received 11 December 1997 and in revised form 25 September 1998)

A combined experimental and numerical investigation is presented of the multiple oscillatory states that exist in the flows produced in a completely filled, enclosed, circular cylinder driven by the constant rotation of one of its endwalls. The flow in a cylinder of height to radius ratio 2.5 is interrogated experimentally using flow visualization and digitized images to extract quantitative temporal information. Numerical solutions of the axisymmetric Navier–Stokes equations are used to study the same flow over a range of Reynolds numbers where the flow is observed to remain axisymmetric. Three oscillatory states have been identified, two of them are periodic and the third is quasi-periodic with a modulation frequency much smaller than the base frequency. The range of Reynolds numbers for which the quasi-periodic flow exists brackets the switch between the two periodic states. The results from the combined experimental and numerical study agree both qualitatively and quantitatively, providing unambiguous evidence of the existence and robustness of these multiple time-dependent states.

1. Introduction

Rotating flows have been studied extensively for a variety of reasons. Their technological applications are many and varied (e.g. centrifugal pumps, turbo-machinery, cyclone separators), and their importance to geophysical flows is manifested over a large range of scales (e.g. tornadoes, hurricanes, ocean circulations). Confined rotating flows have also attracted much interest as a test-bed for contemporary ideas on the role played by finite-dimensional dynamical systems theory on the transition to turbulence (e.g. Gollub & Swinney 1975; Christensen *et al.* 1993; Mullin 1993; Kobine & Mullin 1994; Sorensen & Christensen 1995).

The study presented here is an experimental and computational investigation of the flow in a filled, enclosed cylinder driven by the constant rotation of one of its endwalls. When an endwall (the top endwall here) is impulsively started, a thin Ekman boundary layer is formed that centrifuges fluid radially outwards while drawing fluid in from the interior. The expelled fluid then spirals down the sidewall and is subsequently deflected at the bottom stationary endwall, where it spirals inwards and turns to form a columnar-like vortex centred on the axis. The parameters that determine the flow are the Reynolds number and the aspect ratio of the cylinder. Here, the Reynolds number is $Re = \Omega R^2/\nu$, where Ω is the constant speed of rotation of the endwall, R is the radius of the cylinder, and ν is the kinematic viscosity of the fluid. The aspect ratio of the cylinder is H/R, where H is the height. The earliest published

experimental results on this flow, exhibiting a region of recirculation on the axis, are by Vogel (1968). Such recirculation zones are usually visualized by releasing dye from the centre of the stationary endwall. The dye is advected along the vortex core and spreads out around the recirculation zone. Escudier (1984) extended the results of Vogel, mapping out the steady and unsteady flow regions in $(Re, H/R)$ space. There have been numerous computational studies of this flow (e.g. Lugt & Abboud 1987; Neitzel 1988; Lopez 1989; Sorensen & Daube 1989; Lopez 1990; Daube 1991; Tsitverblit 1993; Sorensen & Christensen 1995; Gelfgat, Bar-Yoseph & Solan 1996), where various aspects of the unsteady motions which exist in different regions of parameter space have been considered.

A numerical study of the periodic flow for $H/R = 2.5$ was conducted by Lopez & Perry (1992) who report the existence of distinct modes of oscillation. One mode consisted of two regions enclosed by the separatrices of the instantaneous streamline pattern periodically coalescing and separating. The other mode consisted of a wave travelling axially from the stationary endwall to the rotating endwall. The modes were also distinguished by the non-dimensional periods of oscillation, $\tau = \Omega T$, where T is the time in seconds required for one complete cycle. Lopez & Perry found $\tau \approx 36$ for $2650 < Re < 3500$, $\tau \approx 36$ and $\tau \approx 28$ for $3500 < Re < 3600$, and a pure period of $\tau \approx 28$ for flows impulsively started with $3600 < Re < 4000$.

Previous experimental results for this flow in the unsteady regime include Westergaard, Buchhave & Sorensen (1993), who obtained particle-image-velocimetry (PIV) and hot-film results for Re ranging from 3000 to 8000 and $H/R = 2$. For the periodic flow at $Re = 3000$, they found the period of the flow to be $\tau \approx 26$ ($\Omega = 4.4$ rad s^{-1}, $T = 5.9$ s). At $Re = 5000$, Westergaard *et al.* reported results that imply $\tau \approx 23$ ($\Omega = 7.8$ rad s^{-1}, $T = 2.9$ s). In their experiments, substantial departures from axisymmetric flow are apparent at Re as low as 3000. The axisymmetric computations of Lopez (1989) for $H/R = 2$ and $Re = 3000$ have $\tau \approx 27$, in agreement with the Westergaard *et al.* experiment. Escudier (1984) reports that the flow remains axisymmetric well into the oscillatory regime, but does not report the oscillation periods for his experiments.

A numerical study of the periodic flow for $H/R = 2.0$ was conducted by Sorensen & Christensen (1995). They observed several regions of hysteresis between periodic flows. Their computed period of oscillation for $Re \approx 3000$ also agrees with the experimental results of Westergaard *et al.* (1993). However, the experiments of Westergaard *et al.* were not sufficiently detailed, nor do they appear to have low enough three-dimensional perturbation levels, to detect the multiple oscillatory states and the associated hysteretic jumps reported by Sorensen & Christensen from their axisymmetric computations. Westergaard *et al.* used a motorized Hasselblad camera with a rate of 1.25 frames per second for PIV measurements. That frame rate is too slow for the fine temporal structures predicted by the numerical computations and revealed in the present experiment.

Recently, Gelfgat *et al.* (1996) looked at the unsteady flow in the neighbourhood of where it first appears using linear stability theory and weakly nonlinear computations. They found that their weakly nonlinear computations agreed very well with the fully nonlinear computations of Lopez & Perry (1992). Here, we extend the investigation into the unsteady flow regime far from the onset of unsteadiness. We present a combined experimental and numerical systematic investigation of this flow in parameter regimes where limit cycle flows and flows on two-tori exist.

In this paper, we study in detail the multiple periodic states that exist for $H/R = 2.5$ over a range of Re where the flow remains axisymmetric. We find, both experimentally and numerically, that three distinct oscillatory states exist in this region. Two of them

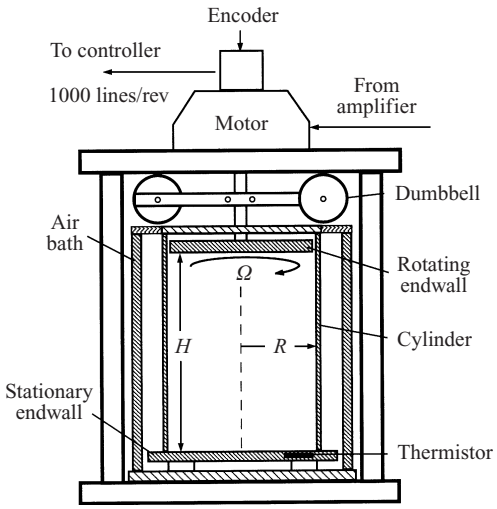

FIGURE 1. Schematic of the experimental apparatus.

are periodic, with fundamental periods denoted τ_1 and τ_2. The third state is quasi-periodic, with a base period denoted τ_3 and modulated by a very low-frequency oscillation. This low-frequency mode is readily detected in the numerics, but due to the relatively shorter data sample length from the experiment, it is not resolved directly from the PSD, other than as side-bands on the fundamental mode. However, plots of time-histories from the experiment clearly show the modulations at frequencies that agree with the numerics. In both the numerics and the experiments, hysteretic jumps between the various oscillatory states are observed and described.

2. Experimental set-up

A schematic of the experimental apparatus is presented in figure 1. The cylinder and both endwalls are made of Plexiglas. The cylinder radius is 9.563 ± 0.005 cm, and the cylinder height can be varied from 14.29 cm to 28.58 cm, giving a range in H/R of 1.5 to 3.0. The rotating endwall is parallel to the stationary endwall to within 0.03° and has a maximum excursion of ± 0.0013 cm at the edge of the disk. The disk is aligned with the axis of the cylinder to within 0.008 cm with a nominal gap between the disk and the cylinder of 0.168 cm. Geometric imperfections, which are always present in an experiment, may take many forms including misalignment of the endwalls, non-circularity of the cylinder and wobble of the rotating endwall. Although the effects of imperfect geometry are applied at the disk frequency, they are most apparent at the 0.028 non-dimensional frequency of the bifurcating unsteady flow. Any wobbling of the disk and/or fluctuations in the disk speed constitute a low-level periodic forcing.

The disk is driven by a PMI Motion Technologies JR16M4CH-1/F9T/ENC servo-motor. A phase-locked loop (PLL) circuit is used to synchronize the motor shaft encoder (1000 pulses/rev) with a clock signal from an HP model 3312A function generator. Due to small, angle-dependent frictional torques present at low Ω, the motor exhibited slight phase variations leading to speed fluctuations on the order of 0.003 Hz. These disturbances were greatly reduced by the addition of a dumbbell-shaped flywheel attached to the motor shaft. When comparing the encoder signal

read by an HP model 34401A multi-meter with the clock signal read by an HP model 5315B universal counter, the encoder signal was found to vary by not more than 2×10^{-7} Hz from the reference signal. Both signals are 1000 times the disk frequency. Hence, the disk frequency remains within 2×10^{-4} Hz of the desired frequency which, for the experiments reported here, is approximately 1 Hz. This very small frequency fluctuation is responsible for a minimum fluctuation of 0.4 in *Re*.

The primary diagnostic technique used in the experiments was imaging of Fluorescein dye (5.4 p.p.m. by weight of Fluorescein powder in 3 : 1 by volume glycerin/water mixture) injected from the bottom endwall. The imperfections cited above cause slight asymmetries in the observed dye patterns. Due to the rotation of the flow through the laser sheet, deviations from axisymmetry appear as apparent oscillations of the flow at a frequency on the order of the disk frequency. In addition care is required to avoid misalignment of the dye injection port with the cylinder axis as this can produce large asymmetries in the injected dye pattern even when the symmetry of the flow field is perfect (Neitzel 1988; Lopez & Perry 1992; Hourigan, Graham & Thompson 1995). Generally, the images of the flow exhibited a high degree of axisymmetry and very little spurious unsteadiness.

The fluid is a 3 : 1 glycerin/water mixture by volume. As noted by Escudier (1984), the viscosity of this fluid is very sensitive to temperature. Viscosity is measured with a Cannon–Fenske routine viscometer over a range of temperatures in the manner prescribed by ASTM Standard Test Methods D 445 and D 446. These data are then fitted to a straight line function of viscosity versus temperature. The accuracy of these viscometers is $\approx 0.35\%$. The temperature in the test section and room are constantly measured during the experiment using thermistors with a precision of $\pm 0.004\,^{\circ}\mathrm{C}$. The curve fit created with the viscometer gives the current viscosity of the working fluid. Taking into account all the measurement errors, the *Re* is known to ± 10, and H/R is known to ± 0.01. Note that these uncertainties are the worst case for estimating the *absolute* values of these parameters. Since the radius of the cylinder remains constant, the *relative* point to point uncertainty in Reynolds number is due only to uncertainties in disk frequency and temperature from which viscosity is interpolated. The relative uncertainty in *Re* is no more than ± 0.7. There is no relative uncertainty for H/R since this is constant during the experiment.

At this point, some comparisons between the current experiment and the experiment of Escudier (1984) are appropriate. First, the size of the step change in *Re* must be considered since this represents the largest disturbance to the flow. The apparatus used by Escudier was capable of a minimum step change in *Re* of ≈ 16 ($\Delta\Omega = 0.11\,\mathrm{rad\,s^{-1}}$, $R = 9.5\,\mathrm{cm}$, $\nu = 0.60\,\mathrm{cm^2\,s^{-1}}$). The continuous background disturbance level cannot be inferred from the specifications presented in his paper. The current experiment is capable of steps in *Re* as small as 0.4, limited by the fluctuations in disk speed. Second, the precision in the *Re* measurement defines how well steps in *Re* are resolved and how well hysteresis events may be captured. Whereas our precision value is 0.7, Escudier has a precision value of at least 13.5 due to temperature-dependent viscosity fluctuations alone.

To prevent temperature gradients in the fluid, the test section is isolated from the room using an air bath. The air bath is a Plexiglas cube with an aluminium bottom. Inside this box, polystyrene insulation material covers five of the six surfaces. The remaining surface is uninsulated for flow observation. With this arrangement, temperature within the cylinder varies very slowly with changing room temperature.

The flow structures are visualized by shining a laser sheet vertically through the centre of the cylinder. When illuminated in this manner, fluid containing Fluorescein

dye released into the vortex core fluoresces showing the meridional behaviour of the flow. Records of the experiments are captured on Hi8 video tape, from which qualitative (images) and quantitative (signal and power spectral density) data are extracted.

In order to reduce the influence of dye injection into the flow, the dye is released at a very low rate (0.02 to 0.11 ml min^{-1}), and since the experimental runs are of long duration (several hours), low levels of dye concentration are used so as to not saturate the working fluid (a 3 : 1 glycerin/water mixture by volume). This, together with the low-power laser used (53 mW He-Cd), results in faint images. To compensate in a non-intrusive manner, the figures are produced by assembling several frames into one frame, resulting in an enhanced total image. While invasive enhancements (e.g. image processing) rely on the interpretation of a single frame from the video, a composite image of several unaltered frames naturally brings out hard-to-see detail. Each individual frame contains information, but since the data are from a low-light video, it is inevitable that some of the detail will be missed. The interpreter, who must judge which areas of the image to highlight or de-emphasize, is taken out of the process. The frame overlaying method can be tailored such that each frame enhances the whole image, building up detail where appropriate. Depending on the particular characteristics of an image, the number of frames used is varied. For very low-light images, up to thirty frames are used; whereas for brighter pictures, five frames may be enough to produce high quality figures. In some cases, the dye contaminates the experiment to a degree that precludes sharp detail.

For the steady flow cases, frames are chosen at random to form a complete image. The periodic flow cases require the use of frames at the same phase of the oscillation. For the quasi-periodic cases only single images could be used. With quasi-periodic oscillations, each frame is unique and combinations of frames would produce confusing ghost images.

Quantitative data were extracted from the video records of the experiment by using a video capture board to digitize the pixel intensity from the sequential, evenly timed frames. Only a small region of each frame, extending from the dye injection port to past the region that included the bubble (instantaneous) stagnation point, 32 (horizontal) $\times 128$ (vertical) pixels, was digitized. These were then passed through a 5×5 pixel Gaussian filter. The first frame in the sequence was used as a reference frame and all subsequent frames were cross-correlated with it. Each resulting cross-correlation matrix was fitted to a Gaussian and the location of its peak was found (interpolating and correcting for biases introduced by fitting a Gaussian peak to an image in motion). Since the dye tends to accumulate at the (instantaneous) stagnation point, this location has the brightest intensity. Hence, the displacement of the Gaussian peak from the origin is a very good estimate of the displacement of the stagnation point from its location in the first frame. This displacement, as a function of time (every frame is 1/30 s apart) provides the time series from which a power spectral density (PSD) is obtained. The data, typically 2^{10} frames long, are windowed by a Hanning window before being fast Fourier transformed.

A certain amount of error is introduced into these data capturing techniques, especially due to the slight non-uniformity of the dye injection, resulting in discrepancies in the calculated position of the dye line. As *Re* is increased, and particularly in the quasi-periodic regimes, the technique becomes less accurate. Nevertheless, the method proved adequately robust for the purposes of mode identification. The strongest factor in the contamination of the experimental data is the precession of the dye line about the hyperbolic fixed point of the upstream bubble. When the video frames are

digitized and processed, the different levels of intensity caused by the erratic motion of the dye line in and out of the laser sheet causes small discrepancies in the apparent motion of the hyperbolic fixed point. Fortunately, most of the undesired motion is in the horizontal and not the vertical direction. The time scale is referenced to the video rate of 30 frames s^{-1}, giving a temporal resolution of $1/30$ s. With a nominal oscillation period of 3 s, the uncertainty in frequency is 0.0037 Hz, or approximately 1.1%. Therefore, all reported experimental times and frequencies, dimensional or non-dimensional, have confidence intervals of $\pm 1.1\%$.

Further details of the experimental techniques and set-up can be found in Stevens *et al.* (1996).

3. Governing equations and computational technique

The governing equations and boundary conditions used are detailed in Lopez (1990) and Lopez & Perry (1992). The numerical results presented here were obtained with essentially the same code as that previously used (Lopez 1990, 1995; Lopez & Perry 1992), which has been extensively tested for grid independence and accuracy in those earlier reports. For the sake of brevity, the details of the numerical scheme and the various tests will not be repeated here. A comprehensive comparison between the present finite-difference code and a spectral-projection code has been presented in Lopez & Shen (1998), along with a discussion of the treatment of the small gap between the stationary sidewall and the rotating endwall.

The equations governing the flow are the axisymmetric Navier–Stokes equations, together with the continuity equation and appropriate boundary and initial conditions. These are written using a cylindrical polar coordinate system (r, ϑ, z), with the origin at the centre of the rotating endwall and the positive-z axial direction being towards the stationary endwall. The velocity vector in cylindrical polars is

$$(u, v, w) = \left(-\frac{1}{r}\psi_z, \frac{1}{r}\Gamma, \frac{1}{r}\psi_r\right),$$

where ψ is the Stokes streamfunction. Subscripts denote partial differentiation with respect to the subscript variable. The corresponding vorticity field is

$$(\xi, \eta, \zeta) = \left(-\frac{1}{r}\Gamma_z, -\frac{1}{r}\nabla_*^2\psi, \frac{1}{r}\Gamma_r\right),$$

where

$$\nabla_*^2 = (\,)_{zz} + (\,)_{rr} - \frac{1}{r}(\,)_r.$$

The axisymmetric Navier–Stokes equations, in terms of ψ, Γ and η, are

$$\mathrm{D}\Gamma = \frac{1}{Re}\nabla_*^2\Gamma,$$

and

$$\mathrm{D}(\eta/r) = \frac{1}{Re}\left\{\nabla^2(\eta/r) + \frac{2}{r}(\eta/r)_r\right\} + (\Gamma^2/r^4)_z;$$

where

$$\nabla_*^2\psi = -r\eta,$$

$$\mathrm{D} = (\,)_t - \frac{1}{r}\psi_z(\,)_r + \frac{1}{r}\psi_r(\,)_z,$$

and

$$\nabla^2 = (\ )_{zz} + (\ )_{rr} + \frac{1}{r}(\ )_r.$$

The boundary and axis conditions corresponding to the flow in an enclosed cylinder driven by the constant rotation of one of its endwalls are: $\psi = 0$ on all boundaries and the axis; $\Gamma = 0$ on all stationary boundaries and the axis; $\Gamma = r^2$ on the rotating endwall; $\eta = 0$ on the axis and $\eta = -(1/r)\psi_{nn}$ on all boundaries, where the subscript n denotes differentiation normal to the boundary. Here, second-order one-sided differences are used for the normal derivatives at the boundary, whereas in Lopez (1990) and Lopez & Perry (1992) only first-order one-sided differences were used.

In Lopez (1990) and Lopez & Perry (1992), the computations were performed using a uniform grid of size $nr \times nz = 61 \times 151$ and a time step of $\delta t = 0.05$. In the present study (as in Lopez 1995), a stretched grid of size $nr \times nz = 66 \times 161$ is employed, given by

$$r = x - a\sin(2\pi x) \quad \text{and} \quad z = (y - b\sin(2\pi y))H/R,$$

where x and y vary uniformly from 0 to 1. The grid stretching parameters a and b have been set to 0.1; this concentrates the grid in the boundary layers on the top, bottom and sidewall, and give a ratio of about one to four between the smallest and largest grid spacing. To account for the smaller grid spacing, $\delta t = 0.02$ was found necessary, but $\delta t = 0.01$ was used for the extra accuracy in the second-order time scheme. This small δt, together with the long time-history data samples, results in highly resolved PSDs of the flow. Typical lengths of records consisted of 2^{18} data points, spaced at $\delta t = 0.01$. The periods obtained from the PSD have three significant figures, and the low-frequency modulation was resolved due to the length of the record being adequate.

The unsteady flows have been characterized by the time histories of two-point values of the azimuthal vorticity, $v_1 = \eta(nr/3, 4nz/5)$ and $v_2 = \eta(2nr/3, 4nz/5)$. The PSDs of the numerical solutions are of the time histories of v_1. The frequencies in this confined, incompressible flow are independent of spatial location; however the power associated with each frequency varies spatially. The different unsteady flows are also characterized by the phase plots of v_1 versus v_2.

4. Results

In the experiments, *Re* was slowly varied and held at several values. Figure 2 shows a typical time history of *Re* over one run. Several runs have been performed to confirm the robustness of the results and to detect different details in different ranges of *Re* accessed by altering the timing of the dye release and altering its concentration. At each level, *Re* was held constant for at least 4500 endwall rotations (i.e. approximately 2.8×10^4 non-dimensional time units).

In both the experiments and the numerics, for $H/R = 2.5$ and *Re* between about 2700 and 4400, three distinct oscillatory solution branches have been observed. For $Re < 3500$, there is a periodic branch, termed the τ_1 branch, with period $\tau \approx 36$ and for $Re > 3500$, there is another periodic branch, the τ_2 branch with period $\tau \approx 28$. Over a range of $Re \in (3200, 3700)$, there is a quasi-periodic branch, τ_3, with a basic period of $\tau \approx 57$ and a much slower modulation period of the order of 1000. The modulation period varies with *Re* (and probably H/R, as do the other periods, but

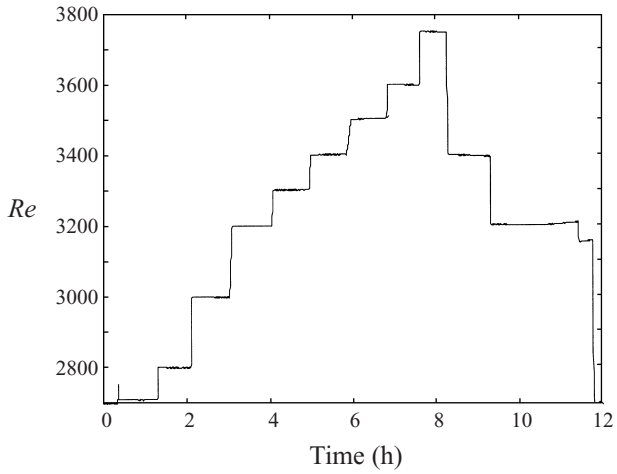

FIGURE 2. Example of the *Re* history during an experimental run.

in this study we have kept $H/R = 2.5$). In the following, various characteristics of these oscillatory flow branches are described.

As the experiment evolved with quasi-steady changes in *Re*, usually starting from an *Re* lower than that where oscillations persist ($Re < 2700$), dramatic changes occurred in the stretching and folding of the lobe structures associated with the unsteady leading recirculation zone. As *Re* was increased, the stretching became more pronounced. This was most evident in the upstream bubble region, with the lobes being stretched farther downstream. Meridional cross-sections of the bubble, illuminated by a laser sheet fluorescing dye in the fluid, clearly indicate the stretching and folding of the dye sheet forming the elongated lobe structures typical of chaotic advection in a time-periodic flow (e.g. $Re = 2800$ in figure 3*a*, which shows a subset of the meridional plane $r < 0.4R$, $0 \leqslant z < 0.5H$).

Upon reaching $Re = 3000$ (figure 3*b*), several observations are made. First, it appears that the dye line emanating from the stationary endwall is precessing about the axis of the cylinder. However, even a small misalignment of the dye injection port with the cylinder axis will cause such apparent asymmetries. The axisymmetric numerical investigations of Neitzel (1988) show how a very small offset in flow tracer origin (from centre to slightly off-centre) can transform a bubble region into spiral streaklines. Hourigan *et al.* (1995) have shown both numerically and experimentally how 'deceptive and illusory flow structures can appear even in the case of *steady* flow in the *absence* of vortex breakdown.' In their experiment, it was noticed that just before the first recirculation bubble appears, the dye line forms a steady spiral streakline even though the dye is injected nominally in the centre of the cylinder. However, once the critical *Re* for the formation of the breakdown had been passed, a steady, axisymmetric bubble was formed. The axisymmetric numerical simulations of Hourigan *et al.* with tracers introduced slightly off the centreline showed the same spiral form before the bubble developed. Naturally, when the tracers are released exactly on the centreline, no spiral streaklines are evident before the formation of the bubble. In our experiment, evidence that the flow is still axisymmetric is provided by the symmetric stretching and folding of the upstream bubble. With much further increases in *Re* (> 4000), this is not the case and asymmetries appear along the entire length of the breakdown structure.

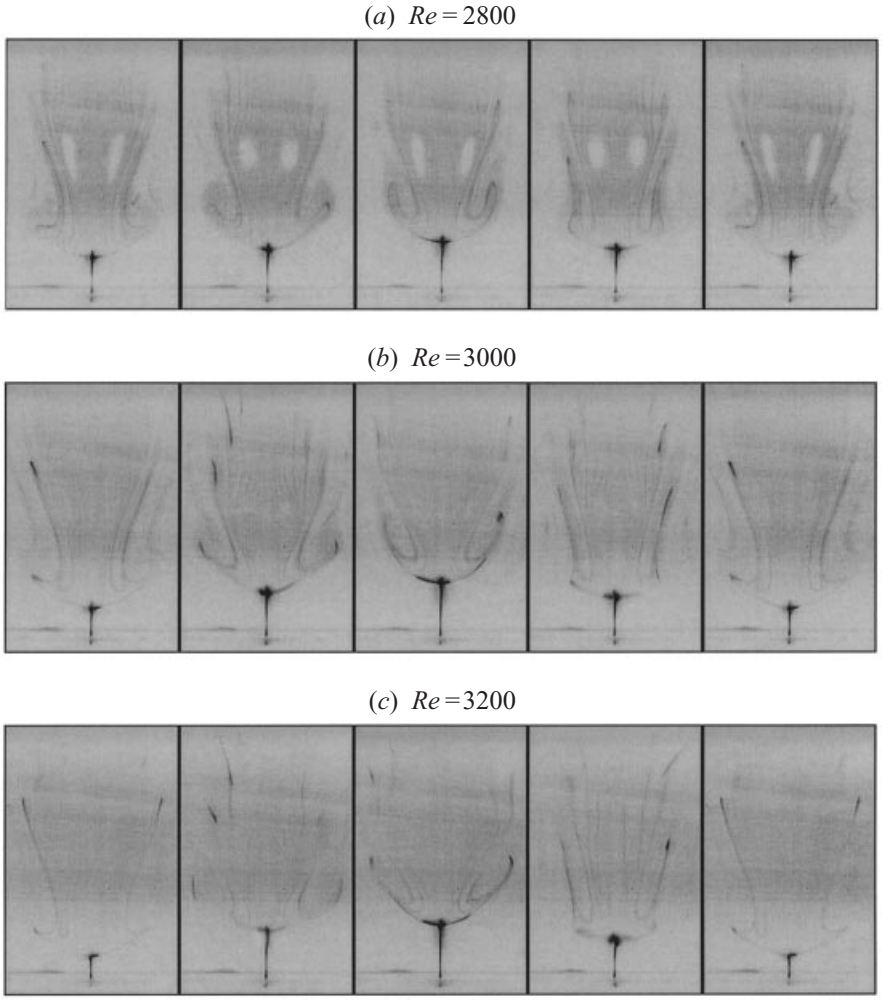

FIGURE 3. Dye sheet released from the centre of the bottom stationary endwall for (*a*) $Re = 2800$, (*b*) $Re = 3000$, and (*c*) $Re = 3200$. Images are equally spaced over a period of τ_1 and are composed of 30 frames each at the same phase. They depict a subset of the meridional plane $r < 0.4R$ and $0 \leqslant z < 0.5H$, illuminated by a laser sheet.

The second observation at $Re = 3000$ is that the regions devoid of dye, presumably delineated by either Kolmogorov–Arnol'd–Moser (KAM) tori or cantori (Rom-Kedar, Leonard & Wiggins 1990; Lopez & Perry 1992), in the downstream bubble have been considerably reduced in size. KAM tori are regarded as boundaries across which fluid cannot pass. Cantori provide only partial barriers to the flow, allowing small amounts of mixing to occur over long periods of time. The KAM tori/cantori of the upstream bubble are no longer detectable by $Re \approx 2750$; periodic orbits have broken up into higher-order periodic islands, and there is increased tangling of the stable and unstable manifolds of the hyperbolic fixed points such that dyed fluid is able to penetrate deeply, but not completely, into the innermost regions of the bubble. By $Re = 3200$, the KAM tori/cantori have essentially disappeared, yet the breakdown structure still oscillates symmetrically as shown in figure 3(*c*).

From another experimental run, the flow at $Re \approx 2700$ fortuitously had the right

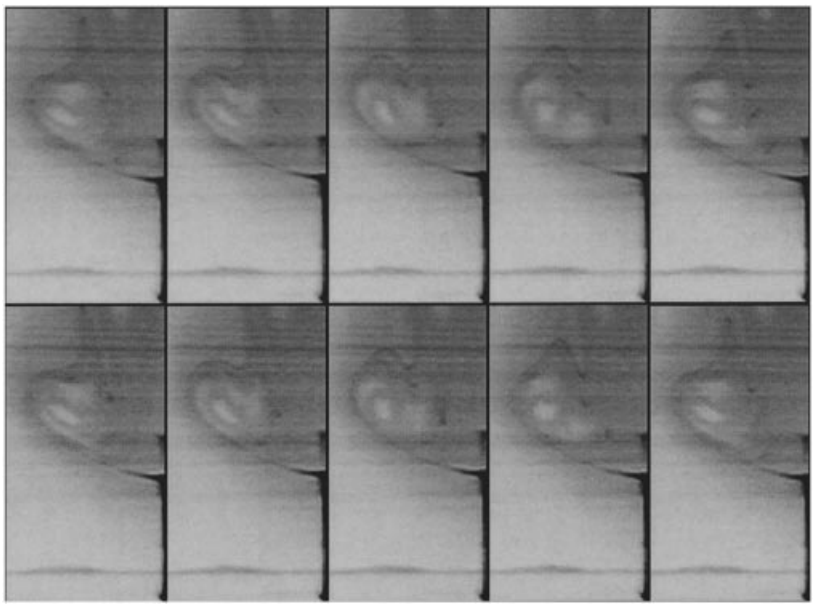

FIGURE 4. Closeup view of the dye sheet released from the centre of the bottom stationary endwall for $Re \approx 2700$ showing a period-one elliptic region surrounded by period-two islands; frames cover two complete τ_1 periods.

amount of dye at the right location in the upstream bubble to show an orbit about the elliptic fixed point to have broken up into two period-two islands. Snap-shots of this flow are presented in figure 4. These are phases covering two complete periods of the flow and clearly show the period-one elliptic region surrounded by the two period-two islands. These features were also observed in this neighbourhood of parameter space in the computations (see figure 6*a* of Lopez & Perry 1992).

Some asymmetries of the breakdown structure appear at $Re \approx 3400$, just before the mode switch from τ_1 to τ_2 takes place in the neighbourhood of $Re \approx 3500$. The non-axisymmetric oscillation is manifested through the slightly uneven stretching of the upstream bubble. One side of the bubble reaches full extension just ahead of the other side. It is not clear whether this asymmetry in the dye streak is real or apparent in light of the discussion above; however, it would not be surprising to find that a non-axisymmetric mode becomes dominant in the neighbourhood of parameter space where there is a switching between different axisymmetric modes. Figure 5 shows the oscillation of the hyperbolic fixed point at $Re = 3500$ along with the power spectral density of the signal for a flow that is fundamentally different from the periodic flows τ_1 and τ_2 observed either side of $Re = 3500$. The power spectrum contains a signal with frequency 0.01732 ($\tau \approx 57$) accompanied by a signal with frequency 0.03505 ($\tau \approx 28$); this is merely a harmonic, but it should be noted that the periodic flow τ_2 has a period $\tau \approx 28$. Some higher harmonics are also detectable. At $Re \approx 3600$, a flow with features in common with this $Re = 3500$ flow is also observed. Another signal, significant with respect to the $\tau \approx 57$ signal, is also apparent at these Re. We estimate this low-frequency modulation to be of the order of 0.001 ($\tau \sim 10^3$), but it is not seen clearly in the experimentally determined PSD as there are not enough cycles to resolve this low frequency. The frequency is evident in the time history shown in figure 5(*a*) as a long-period modulation of the signal. It also appears indirectly in the

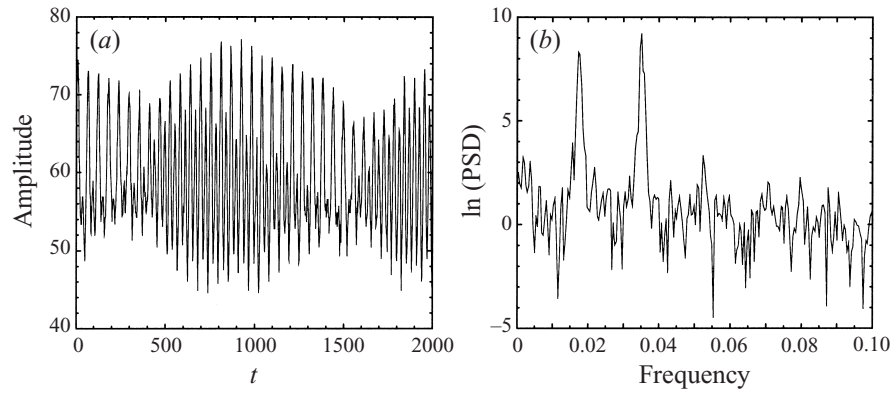

FIGURE 5. $Re = 3500$ (experimental). (*a*) Position of hyperbolic fixed point vs. Ωt and (*b*) power spectral density of signal from (*a*).

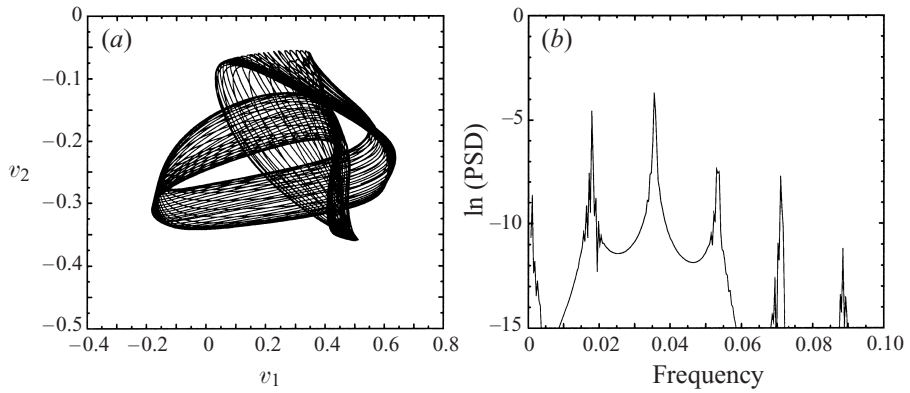

FIGURE 6. $Re = 3500$ (numerical). (*a*) Two torus and (*b*) power spectral density of v_1 for the τ_3 flow.

experiment's PSD as side-bands on the fundamental. These quasi-periodic flows are referred to as τ_3 flows.

The numerical computations were able to continue the τ_1 periodic branch up to $Re = 3485$. With a slight increase in Re to 3500, a τ_3 quasi-periodic flow ensued. Figure 6(*b*) depicts the PSD at $Re = 3500$ obtained from the computations. Having used 2^{18} data points, the PSDs of the computations are much sharper than those of the experiments (figure 5*b*). A comparison between the experimental and the numerical PSDs shows the agreement between the main peaks and the resolution of the low-frequency modulation (frequency ≈ 0.001) from the computations which is clearly seen in the time history from the experiment (figure 5*a*). A representation of this quasi-periodic flow is given by the phase portrait in figure 6(*a*), depicting the two-torus over several cycles of the main frequency (the phase variables used are values of the azimuthal vorticity at two points: $v_1 = \eta(nr/3, 4nz/5)$ and $v_2 = \eta(2nr/3, 4nz/5)$).

The experimental flow exhibits the τ_3 quasi-periodic oscillations up to Re between 3650 and 3675. At $Re = 3675$, the flow switches to the τ_2 periodic flow. The computations were able to follow the τ_3 branch up to $Re = 3730$ by using small continuation steps in Re of size 5. Above $Re = 3730$, only τ_2 oscillatory states were observed in either the numerics or the experiment, up to $Re \approx 5000$. It should be noted that at the

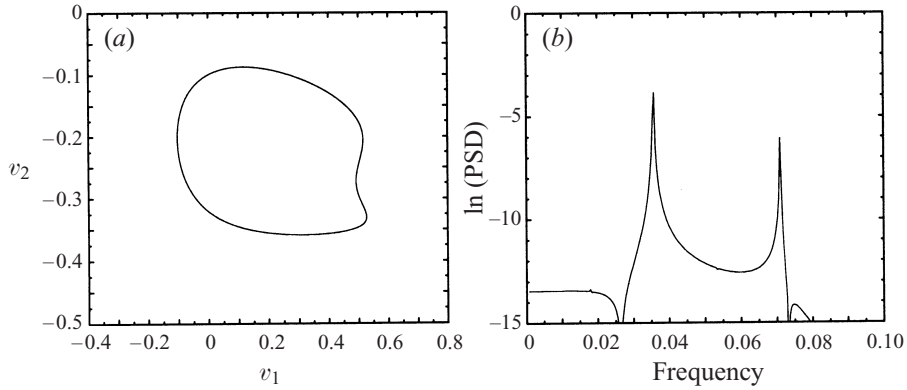

FIGURE 7. $Re = 3500$ (numerical). (*a*) Limit cycle and (*b*) power spectral density of v_1 for the τ_2 flow.

high-Re end of the τ_3 branch, the numerics show that the basic and the modulation frequencies become commensurate and that the frequency of the τ_3 branch is virtually indistinguishable from the frequency of the τ_2 periodic branch, although their phase diagrams, i.e. the azimuthal vorticity associated with each flow state, are very different and provide a means to distinguish the two solution branches (see figure 9).

With a quasi-steady reduction in Re, while on the τ_2 branch, the experiment was able to remain on the τ_2 branch down to $Re = 3625$, while the numerical simulations were able to remain on it down to $Re = 3500$. It is not clear why the experiment was not able to remain on the τ_2 branch for $3500 < Re < 3625$. At both $Re = 3500$ and at $Re = 3600$, the computations evolved to the τ_2 branch following an impulsive start from rest. Figure 7 shows the phase portrait and the PSD for the τ_2, $Re = 3500$ computed solution, which should be compared with the corresponding $Re = 3500$ phase portrait on branch τ_3, shown in figure 6.

Once on the τ_3 branch, the experiment was able to remain on this branch down to $Re = 3200$. Reducing Re to 3150 resulted in a transition to the τ_1 branch. This transition takes place in the numerical simulations when Re is brought below 3225. Figure 8 delineates the range in Re where the various solutions were found to co-exist in the experiments and the numerics, along with their associated periods.

The distinction between a period doubling of the τ_2 flow and a distinct τ_3 flow is now addressed. The observation that the τ_3 flow has a period twice that of the τ_2 flow may suggest that they are related by a period-doubling bifurcation. However, an examination of the phase portraits from the computed solutions reveals that the two flows are not connected by a supercritical period-doubling bifurcation. If they were, then the τ_2 and τ_3 flow phase portraits would merge near the Re above which τ_3 dies out and τ_2 exists ($Re \approx 3730$). Figure 9 demonstrates that this does not happen. Figure 9(*a*) shows the phase portraits of the τ_2 oscillations for $Re = 3500$, 3700, and 4000, and figure 9(*b*) gives the phase portrait of the τ_3 oscillations for $Re = 3730$. The phase portrait of the τ_2, $Re = 3700$ flow is radically different from that of the τ_3, $Re = 3730$ flow. Figure 10 shows phase portraits of the τ_1 flow for $Re = 2705$, 2800, 3200, and 3400 (figure 10*a*), and the τ_3 flow at $Re = 3225$, and figure 11(*a*) shows the phase portrait of the τ_3 flow at $Re = 3400$; the τ_1 and the τ_3 phase portraits do not resemble one another. The computational approach (the solution of the initial value problem) and the experimental approach are not able to unambiguously distinguish between disconnected branches and subcritically connected branches. So,

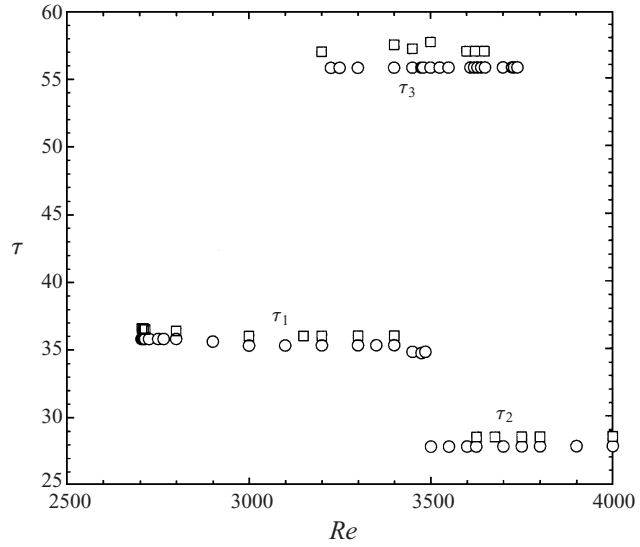

FIGURE 8. Variations of the fundamental periods with *Re* for each of the three oscillatory branches, as determined from the experiments (squares) and the numerics (circles).

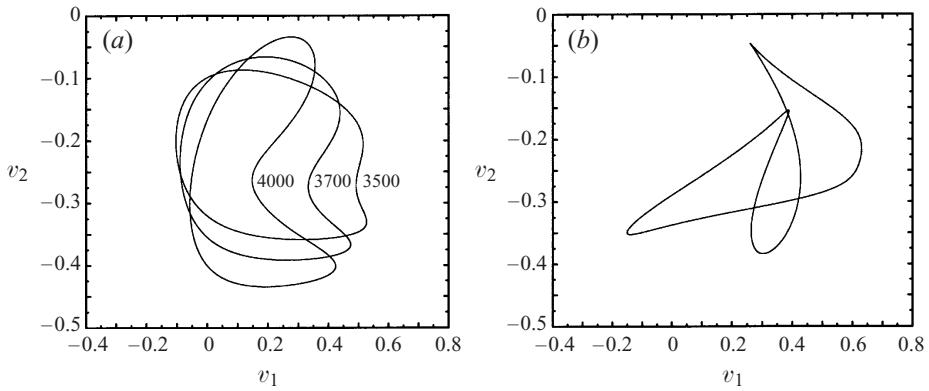

FIGURE 9. (*a*) τ_2 limit cycles for $Re = 3500$, 3700, and 4000, and (*b*) τ_3 limit cycle for $Re = 3730$.

all we can conclude is that none of the three periodic branches found are connected via supercritical bifurcations. Note that any connection between these branches would be of co-dimension 2 or higher (Hopfs from limit cycles, etc.), the analysis of which is non-trivial (Arnold 1988; Wittenberg & Holmes 1997).

The feature that most distinguishes the τ_3 from either the τ_1 or τ_2 periodic flows is its quasi-periodicity, the second frequency being a very low-frequency modulation of the base frequency. The computations show that the modulation dies out as the end of this branch is approached by increasing *Re*. Figure 9(*b*) shows the phase portrait for the τ_3, $Re = 3730$ flow. Although it contains all the frequencies of the τ_2 flow, its phase portrait is not close to any of the τ_2 phase portraits. The modulation frequency is evident for $Re \in (3225, 3700)$ (figure 10*b*). The phase portraits for τ_3 at $Re = 3400$ and 3650 are shown in figure 11. These, together with those for $Re = 3225$ and

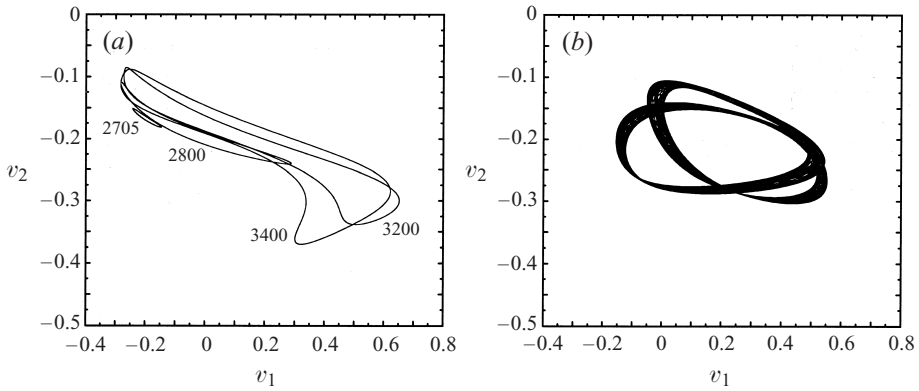

FIGURE 10. (*a*) τ_1 limit cycles for $Re = 2705$, 2800, 3200, and 3400, and (*b*) τ_3 two-torus for $Re = 3225$.

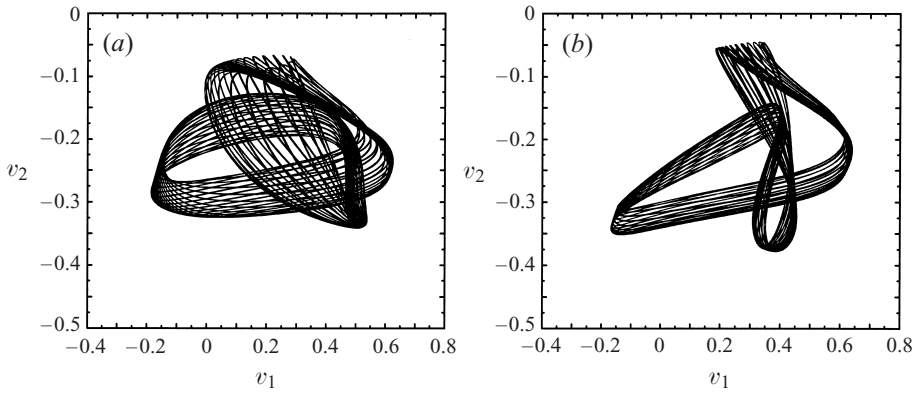

FIGURE 11. τ_3 two-tori for (*a*) $Re = 3400$ and (*b*) $Re = 3650$.

$Re = 3730$, give an indicative picture of how the phase portraits depend on Re along the τ_3 branch.

For Re between 3200 and 3700, we have observed both in the experiments and the numerics three distinct time-dependent flow states, two of them periodic and the third quasi-periodic. Figure 12 is a sequence of images at $Re = 3600$ showing a sequence over time τ_3 (remember that the τ_3 mode is quasi-periodic). This figure shows how evenly the unstable manifolds of the bubble are stretched and folded along the downstream part of the breakdown structure. Also shown in figure 12 is the jagged appearance of the recirculation bubbles which is characteristic of flows with a fundamental period of either τ_2 or τ_3. The overall structure of the flow is very similar to that shown in figure 6(*b*) of Lopez & Perry (1992), corresponding to the τ_2, $Re = 3600$ axisymmetric flow.

For the Re flows discussed so far, any three-dimensional effects are small, allowing extraction of useful quantitative data. At larger Re, however, the three-dimensional perturbations prevent relevant analysis of the flow. The non-axisymmetric stretching of the dye sheet around the upstream bubble leads to a more pronounced precession of the dye sheet about the cylinder axis. This effect is not prominent for $Re < 4000$. The precession causes the dye to appear to be concentrated alternately between the axis of the cylinder and the lobes downstream of the breakdown structure. Actually,

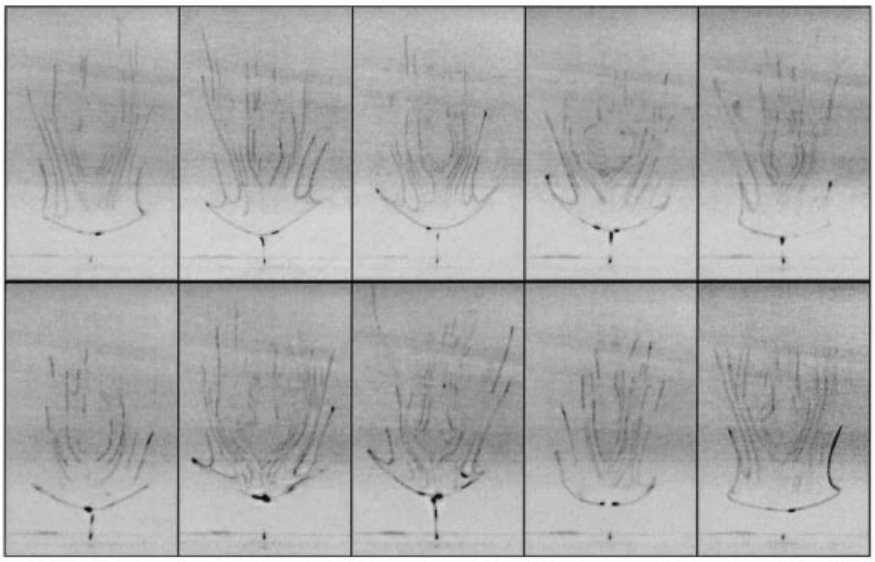

FIGURE 12. Dye sheet released from the centre of the bottom stationary endwall for $Re = 3600$. Images are equally spaced over a time τ_3 of the τ_3 quasi-periodic flow, using one frame per image. The images depict a subset of the meridional plane $r < 0.4R$ and $0 \leqslant z < 0.5H$, illuminated by a laser sheet.

the structure precesses about the centre of the cylinder and therefore wobbles in and out of the laser sheet. When the axis of the structure coincides with the laser sheet, the tree-like structure of the lower-Re flow is visible. However, when the core of the breakdown structure is out of the laser sheet, the fluoresced dye is only located at the edges of the lobes (or even further out from the breakdown core) giving the impression of dye concentrated on the axis of the cylinder. Figure 13 shows different stages of the precession of the structure about the cylinder axis over about 1400 non-dimensional time units for $Re \approx 4400$. By $Re \approx 4700$, the flow has become very three-dimensional and no useful data can be inferred from the images except that the non-dimensional period of the meridional oscillations remains at ≈ 28.6 up to $Re \approx 5200$ (no attempt to estimate the precession period has been made). At these high Re, extraction of relevant data by the techniques used here is very difficult.

5. Conclusion and discussion

This investigation is concerned with the nature of the oscillations of the unsteady flows in an enclosed cylinder with the flow driven by a rotating endwall. Three oscillatory states were found to exist, both in the computations and the experiments, with hysteretic jumps between them. Periodic flow with $\tau_1 \approx 36$ exists for $2700 < Re < 3400$. For $3400 < Re < 3500$, the period of oscillation switches to $\tau_2 \approx 28$. Oscillations with τ_2 exist beyond $Re \approx 5000$, where the flow in the experiment shows departures from azimuthal symmetry. Within the range $3200 < Re < 3700$, a quasi-periodic state with a primary period $\tau_3 \approx 57$ was also found to exist in both the experiments and the computations, and jumps of hysteresis between the τ_1 and τ_3 and the τ_2 and τ_3 states were observed.

Sorensen & Christensen (1995) have also numerically identified multiple co-existing time-dependent branches with hysteretic jumps between them; however, the present

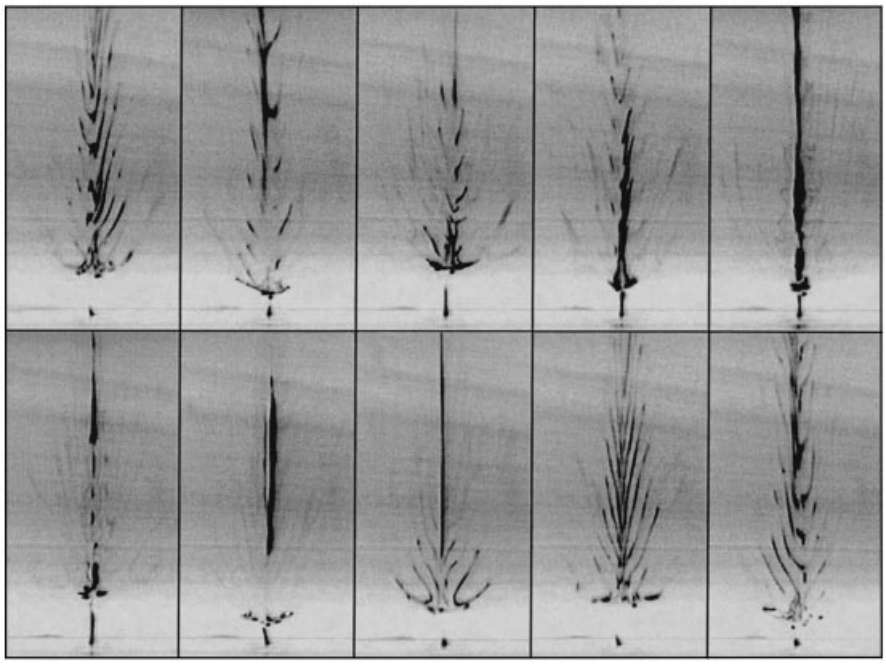

FIGURE 13. Dye sheet released from the centre of the bottom stationary endwall for $Re \approx 4400$ from time $\Omega t = 0$ to 1388. Images are equally spaced and constructed with 1 frame per image.

study is the first to demonstrate their existence and robustness both numerically and experimentally. We have both qualitative and quantitative agreement between the experimental and numerical results for both the periodic and the quasi-periodic flows. The combined numerical and experimental investigation has lead to the unambiguous identification of a new distinct quasi-periodic solution branch that exists over a range in Re bracketing the switch from one periodic branch to the other. The connections between these three time-dependent branches are still not clear and this warrants further investigation. A Floquet analysis of the periodic flows may shed some further insight, as well as giving a clearer picture of how the azimuthal symmetry is broken for Re beyond 3500.

The quasi-periodic (τ_3) flows display some characteristics of homoclinic phenomena, i.e. the period of the modulation $O(10^3)$ is far in excess of the typical timescale of the problem. We were not able to determine the modulation frequency very accurately from the experiment and numerically we observed that it varied considerably over the range of Re for which the τ_3 flows exist, but were unable to determine this variation with much precision. This is still an aspect of the flow that requires further investigation. Similar behaviour has been observed experimentally by Mullin & Price (1989) in Taylor–Couette flow and by Kobine & Mullin (1994) in a variant of Taylor–Couette flow where the outer cylinder is square rather than circular. Kobine & Mullin interpret the observed dynamical behaviour as suggestive of a Šil'nikov-type mechanism (Šil'nikov 1965). Another possible interpretation of the quasi-periodic τ_3 flow stems from the low-frequency periodic bifurcations studied by Davis & Rosenblat (1977), the degeneracy being due to the modulation frequency being much smaller than the base frequency. Braunsfurth & Mullin (1996) have observed similar behaviour in their experiments on convection in liquid gallium. These high-

codimension degenerate Hopf bifurcations have so far only been studied theoretically for a few specific examples in systems of very low dimensions. It would be of great interest to be able to unambiguously determine if these types of low-dimensional dynamics occur in higher-dimensional systems, such as the Navier–Stokes equations. The results presented here provide a preliminary step in that direction.

We would like to acknowledge support by NASA's Graduate Student Researchers Program and the NASA Ames–Stanford University Joint Institute for Aeronautics and Acoustics (JIAA). This work was also partly supported by NSF grants DMS-9512483 and DMS-9706951. The authors would like to thank John Pye and Zeki Çelik for their timely help with the experiments.

REFERENCES

Arnold, V. I. 1988 *Geometrical Methods in the Theory of Ordinary Differential Equations*. Springer.

Braunsfurth, M. G. & Mullin, T. 1996 An experimental study of oscillatory convection in liquid gallium. *J. Fluid Mech.* **327**, 199–219.

Christensen, E. A., Sorensen, J. N., Brons, M. & Christiansen, P. L. 1993 Low-dimensional representations of early transition in rotating fluid flow. *Theoret. Comput. Fluid Dyn.* **5**, 259–267.

Daube, O. 1991 Numerical simulations of axisymmetric vortex breakdown in a closed cylinder. In *Vortex Dynamics and Vortex Methods* (ed. C. R. Anderson & C. Greengard). Lectures in Applied Mathematics, vol. 28, pp. 131–152. American Mathematical Society.

Davis, S. H. & Rosenblat, S. 1977 On bifurcating solutions at low frequency. *Stud. Appl. Maths* **57**, 59–76.

Escudier, M. P. 1984 Observations of the flow produced in a cylindrical container by a rotating endwall. *Expts. Fluids* **2**, 189–196.

Gelfgat, A. Yu., Bar-Yoseph, P. Z. & Solan, A. 1996 Stability of confined swirling flow with and without vortex breakdown. *J. Fluid Mech.* **311**, 1–36.

Gollub, J. P. & Swinney, H. L. 1975 Onset of turbulence in a rotating fluid. *Phys. Rev. Lett.* **35**, 927.

Hourigan, K., Graham, L. J. W. & Thompson, M. C. 1995 Spiral streaklines in pre-vortex breakdown regions of axisymmetric swirling flows. *Phys. Fluids* **7**, 3126–3128.

Kobine, J. J. & Mullin, T. 1994 Low-dimensional bifurcation phenomena in Taylor–Couette flow with discrete azimuthal symmetry. *J. Fluid Mech.* **275**, 379–405.

Lopez, J. M. 1989 Unsteady vortex breakdown in an enclosed cylinder flow. In *Tenth Australasian Fluid Mechanics Conference. University of Melbourne, December 1989. Paper* 9A-1.

Lopez, J. M. 1990 Axisymmetric vortex breakdown. Part 1. Confined swirling flow. *J. Fluid Mech.* **221**, 533–552.

Lopez, J. M. 1995 Unsteady swirling flow in an enclosed cylinder with reflectional symmetry. *Phys. Fluids* **7**, 2700–2714.

Lopez, J. M. & Perry, A. D. 1992 Axisymmetric vortex breakdown. Part 3. Onset of periodic flow and chaotic advection. *J. Fluid Mech.* **234**, 449–471.

Lopez, J. M. & Shen, J. 1998 An efficient spectral-projection method for the Navier–Stokes equations in cylindrical geometries I. Axisymmetric cases. *J. Comput. Phys.* **139**, 308–326.

Lugt, H. J. & Abboud, M. 1987 Axisymmetric vortex breakdown with and without temperature effects in a container with a rotating lid. *J. Fluid Mech.* **179**, 179–200.

Mullin, T. (Ed.) 1993 *The Nature of Chaos*. Oxford University Press.

Mullin, T. & Price, T. J. 1989 An experimental observation of chaos arising from the interaction of steady and time-dependent flows. *Nature* **340**, 294–296.

Neitzel, G. P. 1988 Streak-line motion during steady and unsteady axisymmetric vortex breakdown. *Phys. Fluids* **31**, 958–960.

Rom-Kedar, V., Leonard, A. & Wiggins, S. 1990 An analytical study of transport, mixing and chaos in an unsteady vortical flow. *J. Fluid Mech.* **214**, 347–394.

Šil'nikov, L. P. 1965 A case of the existence of a denumerable set of periodic motions. *Sov. Math. Dokl.* **6**, 163–166.

Sorensen, J. N. & Christensen, E. A. 1995 Direct numerical simulation of rotating fluid flow in a closed cylinder. *Phys. Fluids* **7**, 764–778.

Sorensen, J. N. & Daube, O. 1989 Direct simulation of flow structures initiated by a rotating cover in a cylindrical vessel. In *Advances in Turbulence* (ed. H. H. Fernholz & H. E. Fielder), pp. 383–390. Springer.

Stevens, J. L., Çelik, Z. Z., Cantwell, B. J. & Lopez, J. M. 1996 Experimental study of vortex breakdown in a cylindrical, swirling flow. *Joint Institute for Aeronautics and Acoustics, NASA Ames Research Center/Stanford University; JIAA TR* 117.

Tsitverblit, N. 1993 Vortex breakdown in a cylindrical container in the light of continuation of a steady solution. *Fluid Dyn. Res.* **11**, 19–35.

Vogel, H. U. 1968 Experimentelle Ergebnisse über die laminare Strömung in eine zylindrischen Gehäuse mit darin rotierender Scheibe. *Max-Planck-Inst*. Bericht 6.

Westergaard, C. H., Buchhave, P. & Sorensen, J. N. 1993 PIV measurements of turbulent and chaotic structures in a rotating flow using an optical correlator. In *Laser Techniques and Applications* (ed. R. J. Adrian), pp. 243–265. Springer.

Wittenberg, R. W. & Holmes, P. 1997 The limited effectiveness of normal forms: A critical review and extension of local bifurcation studies of the Brusselator PDE. *Physica* D **100**, 1–40.